GFZ
Helmholtz-Zentrum
POTSDAM

Originally published as:

1 *Transient simulations* of *large-scale* hydrogeological

2 processes causing temperature and salinity anomalies in the

3 Tiberias Basin

4 *F. Magri(1,*), N. Inbar(2), C. Siebert(3), E. Rosenthal(2), J. Guttman(4) and P.*

5 *Möller(1)*

6 (1,*) GFZ German Research Centre for Geosciences, Section 5.3- Hydrogeology,

7 Potsdam, Germany – Corresponding author: fabienma@gfz-potsdam.de

8 (2) Tel Aviv University, The Department of Geophysics and Planetary Sciences, Tel

9 Aviv, Israel

10 (3) Helmholtz Centre for Environmental Research – UFZ, Halle, Germany

11 (4) Mekorot Co. Ltd., Tel Aviv, Israel

12

13 **Abstract**

14   Hot and salty waters occur in the surroundings of the Lake Tiberias. Transient

15 numerical simulations of thermally-driven flow without salinity effects show that

16 mixed convection can explain the upsurge of thermal waters through permeable

17 faults and the high temperature gradient in the Lower Yarmouk Gorge (LYG). It turns

18 out that by including salinity effects, the flow patterns differ from those of a purely

19 thermal regime because heavy brines dampen upward buoyant flow and convective

20 cells. Accordingly, the fault permeability had to be increased to restore a good fit

21 with the measured temperatures. This further supports the hypothesis that the high

22 temperature gradient in the LYG is likely due to fractures or faults in that area. The

23 thermohaline simulations also suggest that the derivatives of relic seawater brines

1

24 are the major source of salinity. Deep brines leaching salt diapirs cannot reach the

25 surface. However, the presence of local shallower salt bodies below the lake can

26 potentially contribute to the salinity of the western spring and well waters, though

27 in very small amount. This is in agreement with geochemical data according to which

28 the major source of the brines of the Tiberias basin represents seawater

29 evaporation brines. Besides being of importance for understanding the

30 hydrogeological processes that salinize Lake Tiberias, the presented simulations

31 provide a real-case example illustrating large-scale fluid patterns due to only one

32 source of buoyancy (heat) and those that are additionally coupled to salinity.

33   **Keywords:** numerical modeling; Lake Tiberias; convection; brine; fault; heat

34 anomaly

35

36   **1. Introduction**

37   Groundwater flow, heat and brine transport processes in large-scale systems

38 are naturally coupled and mutually dependent. Physically, the coupling is mainly

39 through the Darcy law, in which the buoyancy forces and dynamic viscosity depend

40 on pressure, temperature and solute concentration (e.g. Ingebristen, 1999). The

41 consequence of this coupling is that different system behaviors arise (Chen et al.

42 1990). On the basis of a linear stability analysis, Lapwood (1948) shows that, for a

43 porous medium heated from below, free convection is triggered when the value of

44 the Rayleigh number of the medium is higher than a critical number $Ra^{critical}$.

45 Depending on the physical properties of the fluid and geological units, different free

46 convective regimes develop in the form of thermal plumes or fingers (e.g. Nield,

47 1968). In basin systems, free convection is often related to the upsurge of hot

48   springs. For example, Severini et al. (1983) shows that convection with a normal

49   geothermal gradient is capable of producing warm springs in northwestern Virginia.

50   When dissolved solutes are also involved, mass transport within the system is

51   associated with the protrusion of the thermal plumes. In saline environments, this

52   coupled flow is called thermohaline convection. Real study cases are the salt domes

53   of the Gulf of Mexico, where upward brine flow along salt flanks occurs as the result

54   of thermohaline convection (Evans et al., 1991). In the coastal aquifers of western

55   Turkey, free convection in the faults induces seawater intrusion (Magri et al., 2012).

56   Depending on the relative importance of both sources of buoyancy (i.e. heat and

57   salt), solute can be either stabilizing and dampen thermal convection (Diersch and

58   Kolditz, 2002) or enhance gravity-driven flow, as in the case of sinking brine from

59   shallow salt structures (Sarkar et al., 1995; Magri et al., 2009).

60   When thermohaline convection interacts with the regional flow imposed by the

61   topography of the basin, the resulting flow is referred to as mixed convection. Mixed

62   convection is invoked as the main process of ore formation in the McArthur Basin,

63   Australia (Garven et al., 2001). The hydraulic conductivity of the units exerts the

64   major control on groundwater flow, and therefore strongly impacts coupled

65   processes. In this regard, permeable faults provide preferential pathways for mixed

66   convection and discharge of the regional flow. Permeable faults can even allow

67   convection within surrounding units that have a small Rayleigh number (McKibbin,

68   1986).

69   Here a numerical example illustrating the features of large-scale groundwater

70   flow coupled to heat and brine transport in a faulted system is presented. The

71   Tiberias Basin (Fig.1), in the Jordan Rift Valley serves as study case.

3

72   The Jordan Rift Valley is a series of rhomb-shaped pull-apart basins, one of

73   which hosts Lake Tiberias, also known as Lake Kinneret or Sea of Galilee (Fig. 1).

74   Brines are found in springs and boreholes at the shoreline of the Lake, as well as

75   seepages from the lake's floor (Fig. 1). The springs can be classified in clusters

76   according to their location and the local geological settings, as well as to their

77   chemical properties (Table 1). The lake is a major fresh water reservoir for the whole

78   area. Therefore, understanding the driving mechanisms endangering the lake is a

79   crucial aspect to manage this important freshwater resource.

80   Previous numerical simulations based on a W-E cross-section crossing the lake

81   (Gvirtzman et al., 1997a, 1997b) show that topography-driven flow from the Galilee

82   and convection below the Golan coexist (i.e. mixed convection) and can explain

83   different spring behaviors as well as the anomalous geothermal gradient of the area.

84   Similarly, Roded et al. (2013) study the high heat flow below the Lower Yarmouk

85   Gorge (LYG) along a N-S profile at the eastern side of the lake. However, those

86   studies account neither for the salinity effects of relic brines in the units nor for the

87   effects imposed by the presence of a salt dome. Furthermore, in Gvirtzman et al.

88   (1997a, 1997b) faults are not represented numerically, whereas in Roded et al.

89   (2013) the LYG sediments are strongly anisotropic with respect to the hydraulic

90   conductivity to enhance upward heat migration. The studies of Rimmer et al. (1999,

91   2003) and Abbo et al. (2003) are more conceptual: though their transient models

92   successfully explain the seasonal variability of the spring salinity and rate, they are

93   limited to a maximum depth of -900 m, and do not account for temperature effects.

94   These assumptions implicitly exclude any type of deep large-scale flow patterns and

95   source of solute below the Upper Cretaceous aquifers. Hurwtiz et al. (2000a) models

4

96   explain paleo temperature and the transition from a Late Pleistocene salt lake to

97   the actual fresh one. The most recent transient 3D models of Yechieli et al. (2011),

98   from the Geological Survey of Israel, investigate the effects of pumping from the

99   major aquifers on salinity and flow rates of the springs. Yechieli et al. (2011) refers

100 to Kessler's report (2011) on hydrological cells modeling and supplies different

101 forecast for salinity change as consequence of extensive pumping but does not

102 implement deep sources of the saline springs system.

103   The intention of this study is to provide a regional picture of the ongoing large-

104 scale transport processes that control the migration of relic seawater brines in the

105 Tiberias Basin and induce the high temperature anomalies. Adequate equations of

106 state (EOS) for fluid density and viscosity are implemented to account for

107 temperature and salinity dependencies. Furthermore, faults are explicitly modeled

108 using the equivalent porous media (EPM) approach to show the impact of narrow

109 permeable zones on the large-scale flow regimes and on the temperature gradient

110 of the LYG. For the first time, a salt dome based on the interpretation of actual

111 seismic lines is implemented in the numerical models. This setting allows

112 investigating whether the presence of salt structures below the lake can also

113 contribute to the salinity of the springs and wells.

114   The simulation results illustrate the calculated flow paths, as well as fluid

115 temperature and salinity patterns, supported by available temperature profiles of

116 deep wells and spring salinities. In a more general way, the presented scenarios also

117 illustrate the differences between large-scale fluid patterns due to only one source

118 of buoyancy (heat) and those that additionally combine salinity.

119

2. Data

The hydrological data available are mainly based on the yearly reports from the Water Authority of Israel (2012), hydrological surveys (BGR-WAJ, 2001), geophysical and numerical investigations (Yechiely et al., 2011; Kesler, 2011) and several hydrochemical studies in both Israeli and Jordanian sides of the study area, as recalled in this section. The data consist of interpreted geological structures, regional head values, salinity, temperature and flow rates of both springs and wells. They are used to define suitable boundary conditions for the numerical models as well as to qualitatively calibrate the results. Isotopes provide additional constraints on the possible flow paths and groundwater mixing.

2.1. The selected profile and its hydrogeological setting

The selected geohydrological profile starts on the western flank of the Gilboa-Arbel syncline, west to the Lake Tiberias, (Fig. 1). It crosses the western side of the lake, between onshore Fuliya and the offshore Ma'agan springs ("Fu" and "Ma", Fig.1), which are representatives of the Fuliya brine type (see section 2.2) and the Tiberias hot springs ("Ti", Fig.1). The profile runs through the Jordan Rift Valley, which is at that location occupied by the lake. At mid-point between the western and eastern shores, the profile turns to SE and crosses the Ha'on well ("Ha", Fig. 1), the Lower Yarmouk Gorge ("LYG", Fig. 1) and ends in the Cretaceous limestone outcrops of the Jordanian Ajlun Plateau. At its eastern part, the profile is nearly perpendicular to both the geological structure and equipotential lines of the Ajlun Cretaceous aquifer (El Nasser, 1991; BGR, 2001).

Along the studied profile, the groundwater levels vary from -150 m mean sea level (MSL) in the Lower Galilee to -209 m MSL close the lakeshore (Water authority

6

144   of Israel, 2012). The regional water table in the Ajlun Heights reaches elevation of

145   50 m MSL at the end of the profile (BGR-WAJ, 2001). In the LYG, the observed wells

146   are artesian (Siebert et al., 2014).

147   The geological assumptions used to construct the profile shown in figure 2 are

148   based on Inbar (2012) and current interpretation of seismic data from the late 90's

149   (Ben Gay et al., 1997), as recalled here. The Golan Heights and the Ajlun are

150   separated by the LYG (Fig. 2) and are usually described as a continuous ENE-WSW

151   syncline (Meiler, 2011; Roded et al., 2013). According to Shulman et al. (2004), an

152   ancient fault at the LYG explains the huge difference of Jurassic thickness between

153   Ajlun and the Golan Heights, as reflected in the representative cross-section (Fig.2).

154   The ~3 km thick successions of the Triassic (Benjamini et al., 2005) and ~2 km

155   Jurassic sequences in the Lower Galilee (Hirsch, 2005) differ significantly from the

156   much thinner equivalent units in the Ajlun (400 – 500 m each). The Jurassic section

157   east of the Jordan Rift Valley is primarily composed of limestones and marls,

158   whereas the Jurassic in the west also hosts volcanics and dolomite. For that reason,

159   only one unit represents the Jurassic at east, whereas in the west it is subdivided

160   into four "sub-units" (Fig. 2).

161   Above, the Lower Cretaceous Kurnub Group of the Galilee comprises the Tayasir

162   Basalt and the continental sandstone of the Hatira formation (Table 2), attaining a

163   total thickness of nearly 400 m (Rosenfeld and Hirsch 2005). Opposite, in the Ajlun

164   area, the 200 m sequence of mostly coarse-grained Kurnub sandstone indicates a

165   fluvial deposition system with brief marine ingression (Abu Saad and Al Bashish,

166   1996) (Table 2). Accordingly, the different sediment fills significantly vary the

167 physical properties distribution, particularly the hydraulic conductivity (Table 2 and

168 section 3.2).

169   In both regions, intercalations of limestones and marls are building most of the

170 Upper Cretaceous sequence. In the Galilee, the Cenomanian-Turonian sequence is

171 composed mostly of well-bedded dolomites and limestones and while the Turonian

172 and Lower Senonian in the Ajlun is solely composed of limestone (Rosenfeld and

173 Hirsch, 2005; Makhlouf et al., 1996). The Senonian chalks and marls and the Eocene

174 limestones were deposited on a folded terrain, yielding thickness increases in

175 relative position to the synclinal axis (Flexer, 1964).

176   Zemah-1 borehole, located a few kilometers south of the lake ("Z" in Fig. 1),

177 reveals an outstanding thick succession of solid salt interbedded by limestones,

178 clastics and magmatic intrusions (Marcus and Slager, 1985). This unique assemblage

179 of units is named "Zemah Complex" (Inbar, 2012). Following the model suggested

180 by Inbar (2012) and current reinterpretation of seismic data close to the path of the

181 presented geological profile (Fig. 2), it seems that a salt dome is ascending along the

182 western fault of the Jordan Rift Valley. Therefore, it is assumed that below the lake

183 a salt body equivalent in time to the Zemah Complex is present (Fig. 2), the top and

184 depth of which are not known.

185   *2.2. The anomalies: salinity and temperature*

186   Total dissolved solids (TDS) and temperatures of spring and well waters (Table

187 1) are strongly dependent on the seasons. TDS is highly variable, ranging from

188 almost freshwater conditions in the LYG to highly saline outflows in the Tiberias

189 basin. If one compares temperatures and salinity (Fig. 3), three groundwater types

190 can be distinguished: (1) brines from deep wells, (2) springs along the coastline of

8

191 the lake and (3) fresh to brackish waters in the LYG. It can be seen that within the

192 LYG, groundwater is heated up at great depths, and the low TDS indicates that

193 mixing with deep brines plays a minor role (Siebert et al., 2014).

194   Ten meter below the lake bottom, time domain electromagnetic investigations

195 indicate that salinity distribution is not homogeneous (Hurwitz et al., 1999), varying

196 between 11 gL^{-1} and 22 gL^{-1}. Relatively fresh groundwater is detected beneath most

197 of the shoreline because of freshwater advection from regional aquifers along the

198 margins.

199   Overall, very scarce data on TDS is available at depths greater than -800 m MSL.

200 According to the conceptual models of Abbo et al. (2003) the Cretaceous aquifers

201 carry saline waters with chlorinity of 15 to 18 gL^{-1} (up to 48 gL^{-1} TDS), whereas the

202 Eocene aquifers bear fresh water characterized by chlorinity between 0.03 and 0.3

203 gL^{-1} (up to 3.5 gL^{-1} TDS). This finding is in good agreement with the chlorinity-depth

204 profiles by Greitzer (1980). Those profiles further show salinities in deeper units up

205 to 120 gL^{-1} (172 gL^{-1} TDS in the Jurassic). Based on Br/Cl and Na/Cl molar ratios, the

206 back-calculated TDS of deep brine yield to values of more than 300 gL^{-1} (Möller et

207 al., 2012).

208   Groundwater temperatures vary strongly within the same cluster of springs

209 (Table 1). Particularly, in the LYG (Mukhebeh and Hammat Gadder, "Mu and "HG"

210 Fig. 1), the temperature difference between springs and wells that are less than 50

211 m apart can be more than 10 °C. Temperature vs depth profiles at Kinneret 10b

212 ("K10b", Fig. 1) and Mezar ("M" in the LYG, Fig. 1) are shown in figure 4. The K10b

213 well displays an inversion in the temperature trend at about -850 m (MSL). In

214 geothermal systems, this type of anomaly is often associated with cool water

215   flowing through fractures in the surrounding units. Such changes of temperature,

216   however, can also be due to the drilling process or active pumping in the wells.

217   In general, while geothermal surveys indicate that the average conductive heat

218   flux in Israel is rather low, around 40 - 45 mWm^{-2} (e.g. Eckstein and Simmons, 1997;

219   Shalev et al, 2013), the area of the Lake Tiberias is overall affected by heat flow

220   higher than 60 mWm^{-2}, locally reaching 85 mWm^{-2} (Shalev et al., 2008). Particularly,

221   in the southeastern part of the study area, the temperature gradient inferred from

222   deep wells in the LYG is 46 °C km^{-1} (Fig. 4) which is almost twice the average

223   geothermal gradient of the area.

224   Two phenomena are attributed to this anomalously high gradient (Bajjali, 1994):

225   (1) ascent of deep heated groundwater along fractures or (2) heat flow

226   perturbations related to magmatic intrusions. Here, the impact of a fault on the heat

227   transport processes in the LYG is numerically investigated.

228   The numerical models presented here are aimed to understand whether the

229   observed anomalies are related to faults and hydrologic regimes, rather than

230   quantifying the impact of local anthropogenic processes.

231   *2.3. Geochemical evidences for brine movement*

232   Numerous hydrochemical and isotope investigations have been carried out in

233   the study area in order to understand the brine movements responsible for causing

234   the hot saline springs. Mazor and Mero (1969), Gat et al. (1969), Hurwitz et al.

235   (2000a, 2000b), Klein-BenDavid et al. (2004) and Möller et al. (2012) discuss various

236   formations of brines. All studies agree that the observed saline waters are mixtures

237   of meteoric water with some ascending relic brines.

238   Möller et al. (2012) suggests that these relic brine(s) are derivatives of

239   evaporated seawater due to 1000Br/Cl molar ratios of 5.7, which resembles

240   seawater evaporated by about 40% (McCaffrey et al., 1987). The observed relic

241   brines result from the evaporation of seawater that remained trapped in the Rift

242   sediments and adjacent sedimentary rocks during the last Mediterrean

243   transgression. These relic seawater brines are henceforth referred to as source

244   brines (SB).

245   Different mechanisms driving the SB in the basin have been suggested, as

246   reviewed by Simon and Mero (1992). During its ascent, the SB mix with shallow

247   circulating freshwater. The forces that are responsible for upward flow can be

248   induced by compaction of sediments, tectonic stresses or density variations due to

249   geothermal sources (Mero and Mandel 1963; Mazor and Mero, 1969). The latter

250   often implies the generation of convective cells, as shown in numerical models of

251   Gvirtzman et al. (1997a, 1997b). The topography-driven flow imposed by the

252   surrounding heights (e.g. Eastern Galilee, Golan, Ajlun) provides an additional force

253   that flushes deep-seated saline water toward discharge areas (Goldshmidt et al.,

254   1967). Here, the topography-driven flow is also called "regional flow". The same

255   process is referred to as forced convection in Gvirtzman et al. (1997a) or gravity-

256   driven flow in Rimmer et al. (1999, 2003). Rimmer et al. (1999) and Abbo et al.

257   (2003) considered variation of groundwater levels in aquifers showing that the

258   springs discharge and salinity are sensitive to the near lakeshore boundary

259   conditions. Kolodny et al. (1999), Moise et al (2000) and Möller et al. (2012; 2014)

260   discuss leaching by recharge water of residual seawater evaporation brines from

261   pockets.

262   While it is clear that faults play a major role in providing preferential pathways

263   for fluid flow in the Eastern Galilee (Vengosh and Rosenthal, 1994), the presence of

264   deep faulting in the LYG is still an open question. Beside the heat anomaly recorded

265   there (sections 2.1 and 2.2), an additional indication pointing to active faults in the

266   LYG is the high ^{3}He/^{4}He found in the sampled waters (Tsur, 2013; Kaudse, 2014). ^{3}He

267   predominantly originates from the mantle and therefore implies that groundwater

268   interacted with mantle fluids or volatiles rise though open fractures.

269   Depending on the interplay between the above described transport processes

270   and the mixing ratio with the regional flow of freshwater, different types of brines

271   form. Two main branches of brines are distinguishable:

272   (1) Brines along the eastern and southeastern shoreline of the lake and even

273   south of the Yarmouk show low Na/Cl and high Br/Cl molar ratios resembling

274   evaporated seawater. The most prominent brine is the Ha'on brine which best

275   represents the diluted SB. A strongly diluted form of the SB appears in the springs

276   of Hammat Gader ("HG", Fig. 1). Hammat Gader brines are essentially weathering

277   solutions of the basaltic cover in the eastern catchment area. These spring waters

278   contain less than 3% of SB (Siebert et al, 2014). The waters nearby the Mezar deep

279   well ("M", Fig. 1) are recharged over limestones in the foot area of the Hermon

280   Massif (north of the Golan, out of Fig.2) and are very diluted too (Siebert et al.,

281   2014). The brines of Waqed ("W", Fig.1) and nearby Newe Ur wells are the most

282   southern ones that still show high Br/Cl and Mg>Ca but low Na/Cl ratios, typical of

283   evaporated seawater.

284   (2) Brines along the western shoreline of the lake, such as those of the Tiberias

285   hot springs, Fuliya and Tabgha clusters ("Ti,", "Fu", "Ta", Fig. 1), are interpreted as

286 derivatives of the SB (Möller et al. 2012; 2014) because they show similarly high

287 Br/Cl and low Na/Cl ratios like the SB.

288   Fuliya and Tabgha clusters ("Fu", "Ta", Fig. 1) are affected by Tiberias types of

289 water ("Ti", Fig. 1), which suggests northward movement of brines along the

290 syncline. The Golan topography imposes an additional flow of SB below the lake,

291 from east to west (Stiller, 2009).

292   The Na/Cl of SB at the western shore of the lake is slightly enhanced, but still

293 much below one, indicating local leaching of evaporites below the lake. Therefore,

294 it is highly unlikely that the salinity of the observed springs originate from leaching

295 of the Zemach salt plug (Möller et al., 2012).

296   **3.   Modeling Approach**

297   *3.1. Numerical model*

298   Transient simulations of coupled fluid flow, heat and mass transport processes

299 (i.e. thermohaline) are run in order to investigate the possible hydrological regimes

300 developing in the selected profile (Fig. 2**)**.

301   The commercial finite element (FE) software package FEFLOW (Diersch, 2002)

302 is used to solve the partial differential equations (PDE) of thermohaline flow. The

303 strongly coupled system of equations is given in the appendix A. FEFLOW® fully

304 implements variable-density and viscosity form of the Darcy law (Eq. A.1).

305 Polynomial fittings ensure that fluid density (Eq. A6) is dependent on the calculated

306 pressure, temperature and concentration. Only the liquid phase is considered and

307 fluid viscosity (Eq. A7) is pressure independent.

308   The simulations are run over 1 Myr. A semi-implicit time discretization scheme

309   with a maximum time step of 3 yr is used to advance the coupled equations. The

310   simulated time interval of 1 Myr does not represent a specific geological period but

311   allows the simulations to reach a quasi steady-state solution of the problem.

312   The two dimensional approach implies that all processes occur in the vertical x-

313   z plane, thereby neglecting convection parallel to the fault plane, which is the most

314   likely convective mode in fractured media (e.g. Simmons et al. 2008). Convection in

315   the fault plane determines the number of springs along the surface trace of the fault

316   (Lopez and Smith 1996), and further contributes to the migration of both heat and

317   brine. Additional cross-sectional flow cutting the profile is driven by the regional

318   topography that in turn controls the location of discharge areas. Furthermore, at

319   the turning point of the profile (Fig.1 and Fig.2) , it is not possible to apply any mass-

320   balance. While these aspects cannot be accounted in a two-dimensional approach,

321   the 2D patterns illustrated here are still useful indicators of the physical processes

322   and hydrogeological characteristics controlling the temperature and salinity trends

323   observed in the area. At the present state of the research, a 3D structural model of

324   the whole study area is built which will allow investigating the additional impacts of

325   cross-sectional flows and infer salinity mass-balance of the lake.

326   *3.2. Structural setting and properties*

327   The modeled cross section (Fig.2) consists of all units described in section 2.1,

328   except for the poorly constrained stratigraphy below the Triassic at the eastern end

329   of the profile. A basement at 6 km depth closes the model to apply heat flow

330   boundary conditions (Fig.5).

331   The physical properties of each unit (e.g. hydraulic conductivity, storage,

332   porosity and heat conductivity) are given in Table 2. The hydraulic values are mainly

333   adapted from previous numerical investigations (e.g. Gvirtzman et al., 1997a,

334   1997b; Abbo et al., 2003; Roded et al.,2013), conceptual models (e.g. Rimmer et al.,

335   1999) or pumping tests (eg. Bergelson et al., 1998). The model differentiates the

336   main aquifers and aquitards in the vertical direction (z). Furthermore, it also

337   accounts for heterogeneities along the x direction of the profile, as described in

338   section 2.1. By example, the presence of impervious basalt and clays at the base and

339   top of the northern Cretaceous is implemented by assigning a hydraulic conductivity

340   value lower than the one given at the southern side of the profile. The anisotropy

341   ratio of host rocks ($\frac{Kz}{Kx}$) is 0.015, in the range of values inferred by Hurwitz et al.

342   (2000a). By contrast, faults are isotropic, similarly to the investigations of Shalev et

343   al. (2007). Here, the hydraulic conductivity of the faults varies between 30 myr^{-1}

344   (Shalev et al., 2007) and 140 myr^{-1}. The thermal conductivity of the units is an

345   average estimated from the lithological descriptions given in Eckstein and Simmons

346   (1977) and Shalev et al. (2013). The molecular diffusivity value is equal to the

347   chloride self-diffusion coefficient used in the transient salt transport models from

348   Hurwitz et al. (2000b).

349   *3.3. Fault model and mesh*

350   Different well-established approaches exist to model fractures in porous media

351   (e.g. Blessent et al., 2014; Vujević et al., 2014). Here faults are modeled using the

352   Equivalent Porous Media approach (EPM), i.e. permeable units extending from the

353   basement to the top. This choice is dictated by the lack of structural inputs for fault

15

354   geometry that are required to apply other numerical approaches, such as discrete

355   features. Faults are 40 m wide, as in the EPM models of faults in the Dead Sea basin,

356   by Shalev et al. (2007). This fault aperture is very small compared to the kilometer-

357   scale of the flow movements studied here. This configuration is suitable for the EPM

358   approach as this study focuses on the migration of heat and contaminants over large

359   spatial and geological time scale rather than the local prediction of solute exchange

360   at the fault/unit interfaces. The numerical investigations of Abbo et al. (2003)

361   provide an additional example of EPM approach to model mass transport in the

362   faults of the Tiberias area.

363   The "Triangle" algorithm (Shewchuk, 1996) is used to build the finite element

364   mesh. The elements have variable width and preserve the stratigraphic geometries

365   (Fig. 5, zoom). Within the faults, the mesh resolution is approximately 10 meters,

366   i.e. at least four nodes discretize the fault aperture in the x direction. The mesh

367   allows to account for possible buoyant-driven flow within the faults. Element

368   spacing grows gradually from the fault flanks to 50 meters in the surrounding units

369   and basement. This spatial smoothing ensures that (Yang, 2006) : 1) the fault width

370   is in the same order of magnitude of the elements size at the interface, which

371   satisfies the EPM requirements and 2) diffusive-dispersive processes are correctly

372   simulated at the matrix/fault interface.

373   The whole profile comprises approximately 150,000 triangular elements

374   satisfying the Delaunay criterion. Finer meshes did not affect the calculated

375   patterns.

376

377

378   *3.4. Boundary conditions (BC) and initial conditions (IC)*

379   The set of equations describing the thermohaline problem (Appendix A) is

380   solved with respect to the primary variables hydraulic head (h), temperature (T) and

381   concentration (C). The boundary conditions are illustrated in figure 5.

382   - h: Based on the data provided in section 2.2, the head is set as follows:

383   At the top: a constant head (i.e. Dirichlet) is set along the eastern and western

384   sides of the lake. In the Lower Galilee, the regional water vary between -150 m

385   mean sea level (MSL) at the northern ending of the profile to -209 m MSL close

386   the lakeshore. The water table in southern ending of the profile is equal to 50

387   m MSL.

388   In the LYG, h is set slightly above the local topography in order to simulate

389   artesian conditions of the area.

390   Along the lakebed, a transfer boundary condition (i.e. Cauchy, Eq. (1)) accounts

391   for lake and groundwater interactions in the form a Darcy flux $\boldsymbol{q}(t)$ given by:

392           $$\boldsymbol{q}(t) = L(h_{ref} - h)\boldsymbol{n}$$ **Eq. (1)**

393   where the reference head h_{ref} is -210 m MSL (average lake level) and the

394   coefficient of leakage L is $4e^{-2}$ yr^{-1} as estimated by Stiller et al., (1975). $\boldsymbol{n}$ is the

395   vector normal to the top surface of the profile.

396   No groundwater flow (i.e. Neumann) is allowed through the lateral boundaries

397   of the profile.

398   - T: At the top, a heat transfer (i.e. Cauchy) with a reference temperature

399   T_{ref} of 20°C is assigned. This open boundary condition (Eq. (2)) allows heat

400   outflow through the surface, governed by

401           $$\boldsymbol{q_T}(t) = \emptyset_T(T_{ref} - T)\boldsymbol{n}$$ **Eq. (2)**

17

402   where the heat transfer coefficient $\emptyset_T$ = 0.13 WmK^{-1} corresponds to the heat

403   conductivity of the Quaternary sediments (Table 2) divided by the

404   representative element height (10 m). Accordingly, the calculated temperature

405   T can increase at the locations where thermal springs are predicted by the

406   model.

407   At the basement, previous simulations used variable heat fluxes ranging from

408   60 mWm^{-2} to 72 mWm^{-2} (Gvirtzman et al., 1997a) or 50 mWm^{-2} to 100 mWm^{-2}

409   (Roded et al., 2013) over different portions of the studied profiles, in order to

410   reflect the observed thermal anomalies of the area. Since the numerical

411   investigations presented here mainly focus on the impact of faults on

412   redistribution of heat and brine in the system, a constant heat flux is set along

413   the whole profile basement. Specifically, an undisturbed basal geothermal flux

414   (i.e. Cauchy) of 60 mWm^{-2} is set at the bottom of the model. This allows inferring

415   to which extent the observed temperature and salinity anomalies result from

416   hydrogeological features of the basin, such as circulation of thermal waters

417   through faults, rather than imposed deep crust anomalies.

418   Lateral boundaries of the cross-section are insulated (i.e. Neumann).

419   - C: A Cauchy mass transfer boundary condition (Eq. (3)) is set at the top,

420   analogously to the head and temperature boundary conditiona (Eq. (1) and Eq.

421   (2)). The mass flux $\boldsymbol{q_C}(t)$ is given by

422      $$\boldsymbol{q_C}(t) = \emptyset_C\big(C_{ref} - C\big)\boldsymbol{n}$$ **Eq. (3)**

423   The concentration reference C_{ref} is 0,22 gL^{-1} at the lake (average lake salinity)

424   and 0 gL^{-1} along the remaining portions of the top profile. The mass coefficient

425   transfer $\emptyset_C$ is 4e^{-2} yr^{-1}.

426   A constant concentration of 300 gL^{-1} is set at salt dome (UZC). FEFLOW® cannot

427   account for dissolution of salt and therefore the shape of the UZC does not

428   change with time.

429   The transient simulations are initiated as follows (Fig. 5):

430   -   *h*: The initial conditions for hydraulic head are derived from steady state

431   simulations of groundwater flow.

432   -   *T*: As for the hydraulic head, the initial temperature profile is purely conductive

433   (Fig. 5, top). Because of the high thermal conductivity of the UZC (Table 2),

434   isotherms are slightly bending at the salt edges. This phenomenon is very

435   common in geothermal basins hosting salt domes (e.g. O'Brien and Lerche,

436   1988).

437   -   *C*: In the paragraph 4.2, thermally-driven flow is coupled to brine

438   transport. For this purpose, based on the data and considerations described in

439   sections 2.2 and 2.3, an initial salinity condition is set to reflect the presence of

440   the relic source brines (SB) resulting from seawater evaporation , as illustrate in

441   figure 5 (bottom): the concentration increases from freshwater conditions

442   within the top aquifers (Eocene) to 250-300 gL^{-1} in the basement and UZC. This

443   assumption certainly does not reflect paleo-salinity conditions of the area nor

444   correctly represents the Plio-Miocene SB. Nevertheless, it allows studying the

445   impact of faults, heat and regional flow on the migration of the relic seawater

446   SB

447

448

449   **4.   Results and discussions**

450   Models of fluid transport processes over basin-scale and geological time periods

451   like those presented here cannot be calibrated and verified for temperature and

452   salinity at a given time and location. Nevertheless, the results are qualitatively fitted

453   to the temperature-depth profiles of the wells and the salinity ranges of the springs

454   described in section 2, by testing different fault permeability. This kind of "regional

455   calibration" allows investigating the major hydrogeological processes that control

456   the migration of heat and brine in the system.

457   *4.1. Scenario 1: Effects of geothermal flux on flow and temperature anomalies*

458   Following previous numerical studies of the area (e.g. Gvirtzman et al., 1997;

459   Roded et al., 2013), only equations A.1 to A.3 are solved here, i.e., no brine transport

460   is computed. Accordingly, fluid density and viscosity (Eq. A.6 and Eq. A.7) are not

461   dependent on the concentration C. This simplifying assumption is made to directly

462   compare the findings with those from previous studies and later infer the impact of

463   salinity (section 4.2).

464   Velocity and temperature fields resulting from the coupled fluid flow and heat

465   transport process are illustrated in figure 6 (top). In this scenario, all faults except

466   the minor one below the lake are permeable, with a hydraulic conductivity of 30

467   myr^{-1}, like in the simulations from Shalev et al. (2007). Two major independent flow

468   fields can be distinguished:

469   (1) A topography-driven flow (or regional flow) below the Lower Galilee and

470   southeastern heights discharges groundwater through the Turonian/Cenomaniam

471   and Upper Eocene units, respectively. Therein, the velocity ranges between 0.4 myr^{-}

472   ^{1} to 1 myr^{-1}. Springs exhibit peak velocities between 3 myr^{-1} and 5 myr^{-1} at the fault

473 traces that border the lake and in the discharge area of the LYG. A sensitivity analysis

474 showed that springs flow rate per meter width reaches 3600 m^3yr^{-1} when the

475 hydraulic conductivity of the elements at the top of the fault is 400 myr^{-1} (e.g. gravel-

476 sand). Assuming springs to discharge over a km-long shoreline, the inferred spring

477 fluxes are in the same order of magnitude of the monitored ones.

478   (2) Different deep-seated convective flows are separated from the upper

479 regional flow by the major aquitards. A squeezed cell develops in the Jurassic Nirim

480 ("JN", Fig. 6) within the northern part of the profile. The calculated Rayleigh number

481 of the Jurassic Nirim is much smaller than the critical value of the onset of thermal

482 convection, calculated according to the theory of Nield (1968). However, in the

483 presence of permeable faults, it is known that convection occurs also in units with

484 subcritical Rayleigh properties (McKibbin, 1986). Channeled buoyant flow in the

485 faults induces groundwater in the surrounding units to flow either in a convective-

486 like mode or directly toward the faults, like in the overlying Jurassic Zohar ("JZ", Fig.

487 6). Darcy velocities of a centimeter per year characterize this cellular regime, which

488 is one to two orders of magnitude weaker than the upper regional flow. In contrast

489 to the fault-induced groundwater flow in the Jurassic units at the northern side,

490 thermal buoyant forces generate Rayleigh convective patterns in the LYG and Golan

491 Heights. Two cells circulate groundwater below the Senonian aquitard at a

492 maximum velocity of 0.1 myr^{-1}. This is due to the presence of more permeable and

493 thick cretaceous horizons at depths which Rayleigh number is higher than the

494 estimated $Ra^{critical}$. As a result, the heat flow destabilizes the fluid density: the

495 vertically elongated cell below the Golan forces groundwater to descend from the

496 Upper Turnonian units (-1 km depth MSL) to the Lower Jurassic (-3 km depth MSL),

21

497   while deep groundwater rises mostly through the LYG fault and partly through the

498   Ha'on fault, at velocities close to 2 myr^{-1}. In this respect, deep-reaching faults

499   provide the only hydraulic connection between the deep convective systems and

500   the shallower regional flow, allowing thermal water to ascend from depths of -3 km

501   MSL. Discharging springs result from the interaction of these two regimes

502   supporting the chemical data that spring waters are a mixture of deep thermal

503   water and shallow groundwater.

504   The regimes described above strongly affect the temperature distribution (Fig.

505   6, bottom). At the northern part of the profile, the thermal water ascending to the

506   surface along the fault flanking the lake generates an elongated heat plume. Hot

507   groundwater is drained from the Jurassic units and flows out of the system at

508   temperatures between 50 °C and 60 °C. The tip of the heat plume spreads also

509   laterally toward the northern side of the profile because of the presence of open

510   faults that partly capture the ascending flow (Fig. 6, zoom). Therefore, groundwater

511   temperature can either vary of several degrees over the lateral temperature

512   gradient or decrease with depth. A simulation in which buoyant forces are not

513   computed (i.e. $\rho^f = \rho_o^f$ in Eq.(A.2)) prevents any heat plume to ascend from depths,

514   but reveals a local regional flushing through faults (i.e. advection) of groundwater

515   from Upper Turonian/Eocene formations, allowing a maximum spring temperature

516   of 32 °C. Both calculated temperatures are in agreement with the monitored spring

517   temperatures (Table 1), suggesting that thermal buoyant flow in the faults and

518   advection by regional flow are both possible heat transport mechanisms.

519   Below the LYG, the two convective cells generate an upwelling of deep

520   groundwater into the LYG fault, and a downwelling of colder water in the fault

521 below the Golan. Spring temperature in the discharge area of the LYG is 35 °C owing

522 to the presence of a strong regional flow in the upper Eocene unit that cools down

523 the rising thermal plume. The small upwelling observed at Ha'on is due to the local

524 groundwater outflow from the neighboring Golan, as also indicated by a spring

525 temperature of 30 °C.

526   The temperature-depth profiles along two boreholes, as located in Fig.6, show

527 a good fit with available well data (Fig. 7, red crosses and circles). The temperature

528 inversion observed at K10b well (red circles) is due to the spreading of the heat

529 plume toward neighboring permeable faults, as previously explained (Fig. 6, zoom).

530 If the fault at the western side of the K10b well is impervious, the heat plume cannot

531 spread laterally, leading to a linear vertical temperature gradient (Fig. 7, yellow

532 circles).

533   In the LYG (Fig. 7, red crosses), the presence of the fault allows the temperature

534 gradient to be steep even under normal basal heat flow conditions. Interestingly,

535 without the LYG fault, the convective plume persists and the temperature trend is

536 preserved (Fig. 7, yellow crosses). However, since hot water is not anymore

537 channeled upward, the calculated temperatures are lower compared to the case

538 with fault (Fig. 7, red crosses).

539   Gvirtzman et al. (1997) models display similar patterns below the Golan. The

540 simulations of Roded et al. (2013) display a thermal plume discharging upward in

541 the LYG. However, those results are inferred from simulations that do not account

542 for salinity effects, as discussed in the next section.

543

544

4.2 Scenario 2: coupling with salinity

546   Here the fully coupled system of flow, heat and mass (i.e. salt) transport

547   processes is solved (Eq. A.1 to A.7). The EOS account for pressure, temperature and

548   salinity effects. It is worth recalling that an initial salinity distribution is set to model

549   the SB that originally saturates the units. It is assumed that the TDS of the SB

550   increases from freshwater conditions at ground level, to 300 gL^{-1} at the salt dome

551   (Fig. 5 bottom, and section 3.4).

552   When the hydraulic conductivity of the faults is 30 myr^{-1} (as in the purely

553   thermal simulations, paragraph 4.1), this initial salinity distribution overwhelms the

554   convective regimes in the deep units and prevents any thermal buoyant flow in the

555   faults (i.e. no thermal plume) that was previously observed in the scenario without

556   salinity (section 4.1). Salinity also increases the dynamic viscosity of the brine (Eq.

557   A.7) and therefore reduces the effective hydraulic conductivity of the sediments (Eq.

558   A.5). As a result, the only observable process is the topography-induced flow that

559   flushes SB at the lake shores and through the LYG.

560   A sensitivity analysis reveals that by increasing the hydraulic conductivity of the

561   faults to values ranging between 90 myr^{-1} to 140 myr^{-1} triggers buoyant flow and

562   best fits the measured temperature data (Fig. 7, green crosses and circles). The

563   results of this scenario are illustrated in figure 8 and can be compared with figure 6

564   (no salinity scenario, section 4.1). The western fault flanking of the Jordan Rift Valley

565   and the LYG fault remain the preferential pathways for upward flow of thermal

566   water. While the flow patterns of the topography-driven flow in the upper units is

567   qualitatively similar to the previous case (section 4.1- point 1), the deep convective

568   regimes (section 4.1- point 2) are different. The cell below the Galilee Mountains

569 develops into the Upper Jurassic Zohar ("JZ", Fig. 8), creating a wide stagnant zone

570 below it (Fig. 8). Hence, thermal waters that ascends along the western fault of the

571 Jordan Rift Valley originate at depths between -2 km MSL. Also at the southern side

572 of the profile, the cellular patterns are different from those calculated in a purely

573 thermal regime (compare Fig. 8, top and Fig. 6, top). The flow below the Ajlun is not

574 anymore convective but directed toward the LYG fault. Groundwater in the

575 overlying Turonian unit is not fully drained by the Ha'on fault and can flow westward

576 below the lake into the discharging fault. Darcy velocities characterizing this

577 movement into the sedimentary fill are however very slow, at maximum 1 cmyr^{-1}.

578 Geochemical evidences, as explained in section 2.3 (point 2), also request this brine

579 movement. In its lower part, the cell stretches toward the salt flank where

580 downward flow is dominant.

581 Salinity and temperature distributions resulting from these hydrologic regimes

582 are illustrated in figure 8 (bottom). The evolution of the SB can be inferred by

583 comparing Fig. 5 (bottom) and Fig. 8 (bottom). The steep syncline structure of the

584 units in the Lower Galilee enhances gravity-driven flow, which flushes the relic

585 brines. Overall, wide areas of diluted SB bearing less than 0.1 gL^{-1} TDS characterize

586 the Upper Cretaceous units in direct relation to the topography-driven flow below

587 the major Heights. Salinities are 2.5, 6 and 1.5 gL^{-1} at the western shore spring,

588 Ha'On well and LYG springs, respectively. The concentration profile exhibits areas of

589 diluted brine at the eastern shoreline, because of the inflow of freshwater from the

590 surrounding regional flow, as observed by Hurwitz et al. (1999). Accordingly, by

591 decreasing the hydraulic conductivity of the cover basalt, the salinity near Ha'on

592 increases to the monitored values (Table 1.).

593   Brine migration is strongly coupled with the heat transport in the faults. As

594   explained in the previous section, neighboring open faults can capture ascending

595   thermal waters (Fig. 6, zoom). As a result, the brine plume at the northwest side of

596   the lake spreads 2 km inland over the lateral temperature gradient (Fig. 8, zoom).

597   Therein salty groundwater is a mixture of relic seawater (SB) flushed by the

598   freshwater regional flow through the northern Turonian units and buoyant thermal

599   brines that reach the surface through the faults. Those brines likely contain

600   additional fingerprints of dissolved evaporites lifted up either through the fault

601   adjacent to the diapir crest or transported by the S-N flow above it (Fig. 8, top). By

602   contrast, on the opposite side of the diapir flank, gravity-driven flow constrains

603   heavy brine into the deep Jurassic/Triassic units. The thermal plume in the LYG has

604   the potential to drive relic SB from Turonian/Senonian units toward the gorge. This

605   upward flow is further enhanced by the regional flow from the Ajlun. As a result,

606   the plume is narrow (i.e. diluted) and the isotherms at the southern side of the

607   profile are flat compared to those resulting from the purely thermal regime (Fig. 6).

608   Contrarily to the previous scenario, without the LYG fault no thermal plume

609   develops: heavy brines endure a lateral/downward migration at depths and the

610   isotherms are close to the conductive regime.

611   *Impact of salt diapir and faulted lakebed*

612   A simulation initiated with freshwater conditions (i.e. 0 gL^{-1} everywhere except

613   the salt dome) is run in order to infer the impact of brine diffusion from the salt

614   diapir. The results show that no brine reaches the surface. Only a light salty plume

615   above the salt crest diffuses below the western shore of the lake with maximum TDS

616   of 0.2 gL^{-1}, which supports the hydrochemical evidence of leached evaporites in the

617 wells along the western side of the lake (Möller et al., 2012) and not in Ha'On well.

618 The presence of a permeable fault crossing the lakebed does not strongly affect the

619 large-scale patterns of heat and salt transport within the profile. Only a local effect

620 on the salinity distribution below the lake is observed. The calculated concentration

621 of the offshore spring is 6.7 gL^{-1}, and its temperature is 22 °C. Because of the

622 westward flow in the sedimentary fill, additional SB and salty water diffusing form

623 the salt crest can reach onshore springs. Consequently, the calculated concentration

624 of the western spring increases to 3 gL^{-1}.

625 The 2D limitation of these models prevents the assessment of additional brine

626 and heat flow from cross-cutting faults, such as from Tiberias to Fuliya, and

627 transversal regional flow. Also, the models do not account for overpressured

628 aquifers that can further increase upward heat and brine migration. These two

629 aspects could explain the extremely high salinity of the Tiberias springs (Table 1),

630 which cannot be reproduced by the simulations.

631   5.   Summary and conclusions

632 Available hydrochemical data indicate that the thermal springs in the Tiberias

633 Basin (TB) mainly discharge deep waters that represent diluted source brines (SB),

634 resulting from evaporation of seawater of the last Mediterranean transgressions.

635 Geothermal data and geological considerations on the TB suggest that fault-

636 controlled hydrothermal processes generate the anomalous temperature

637 inversions observed at depths and the upsurge of hot/saline spring waters. The

638 variable salinity of the springs is due to the changing rates of the freshwater

639 topography-driven flow (regional flow).

640   First, numerical simulations of coupled heat and flow processes (without salinity

641   effects) are run over a representative geological profile of the area to gain insights

642   into heat transport in the system (section 4.1, Fig.6). The hydrothermal behavior of

643   the system is the expression of two different large-scale flow patterns separated by

644   the Cretaceous aquitards (Table 1). (i) A topography-driven flow rapidly discharges

645   groundwater at lowlands. In this regional movement, groundwater gains heat while

646   flowing through the Turonian and Eocene units. The springs temperature is around

647   30°C. (ii) The underlying convective regimes are either induced by ascending hot

648   waters in the faults or by density instabilities in the thick permeable Cretaceous

649   units below the LYG. Both types of cells are observable under an undisturbed basal

650   heat flow regime of 60 mWm^2, which is a representative value for the study area.

651   Buoyant flow of thermal waters in the faults can explain temperature higher than

652   30 °C observed at some springs. In this regard, the results are in good agreement

653   with available data (Fig. 7, red). Temperature inconsistencies recorded at the same

654   depth of different wells may reflect the diverse hydrogeological behavior of the

655   surrounding faults. Besides permitting upsurge of hot water, permeable faults

656   induce radial temperature gradients by partly capturing upward groundwater flow

657   (e.g. K10b well), or by allowing recirculation of cool groundwater from shallower

658   units, as in the fault below the Golan Heights (Fig. 6, zoom). It turns out that in a

659   freshwater environment the thermal plumes in the LYG form even without a fault.

660   This is due to the convective downwelling of cool water in the Golan Heights that

661   pushes hot water toward the LYG.

662   In the thermohaline simulations (section 4.2), an initial salinity representing

663   evaporated seawater brine, the source brine (SB), is implemented (Fig. 5, bottom).

664 It turns out that only the regional flushing in the shallow units is observable and the

665 deep heat transport is close to conduction, overwhelmed by the initial salinity

666 distribution. Topography-driven flow alone cannot support the anomalous

667 temperature profiles observed in the wells nor springs temperature above 30°C. The

668 anomalies are numerically reproduced by further increasing the permeability of the

669 faults (Fig. 7, green and Fig.8, zoom). Besides transporting heat, permeable faults

670 permit the regional flow to dilute and flush the SB. In this regard, the hydraulic

671 conductivity of the Quaternary sediments and the basalt cover also plays an

672 important role on the discharge rates of the springs. The springs of Hammat Gadder

673 in the LYG discharge highly diluted SB. By contrast, at depth below -2. 5 km MSL,

674 areas of highly saline and quasi-stagnant SB, as well as downward gravitational flow

675 from the salt body, characterize the whole profile.

676 Northwestward groundwater flow may have the potential to transport small

677 amount of salt from shallow salt bodies below the lake. Instead, no brine plume

678 from salt diapir reaches Ha'on, at the eastern side of the lake.

679 To some extent, the presented results are illustrative of the present day

680 situation because of the lack of paleo data and the static nature of the structural

681 features of the model. Nevertheless, the results provide the basis to extend the

682 models to a three dimensional scenario. 3D models of selected areas of the TB are

683 currently being build and will allow studying the different convective modes in the

684 fault planes, that can explain the complex brine movements along the master faults.

References

Abbo, H., Shavit, U., Markel, D., Rimmer, A., 2003. A numerical study on the influence of fractured regions on lake/groundwater interaction; the Lake Kinneret (Sea of Galilee) case. Journal of Hydrology, 283(1–4), 225-243.

Abu Saad, L., Al Bashish , M., 1996. Surface and subsurface lithostratigraphic relationships of the Kurnub Sandstone Group in Jordan. Subsurface Geology, Bulletin 9, pp. 76.

Bajjali, W.T., 1994. Recharge and regional circulation of thermal groundwater in northern Jordan using isotope geochemistry. Ph.D Thesis, University of Ottawa, Canada, Ottawa, Canada, 211 pp.

Baijjali, W., Clark, I.D., Fritz, P., 1997. The artesian thermal groundwaters of northern Jordan: insights into their recharge history and age. Journal of Hydrology, 192(1–4), 355-382.

Ben-Gay, Y., Reznikov, M., 1997. Multichannel seismic survey at the Sea of Galilee. 733/167/97, Geophysical Instittute of Israel.

Benjamini, C., Hirsch, F., Eshet, Y., 2005. The Triassic of Israel. In: J.K. Hall, V.A.K., F. Hirsch, C. Benjamini, A. Flexer (Ed.), Geological Framework of the Levant Volume II: The Levantine Basin and Israel. Historical Productions Hall, pp. 331-360.

Bergelson, G., Nativ, R., Bein, A., 1998. Assessment of Hydraulic Parameters of the Aquifers Around the Sea of Galilee. Ground water, 36(3), 409-417.

Bergelson, G., Nativ, R., Bein, A., 1999. Salinization and dilution history of groundwater discharging into Lake Tiberias, Israel. Applied Geochemistry, 14, 91-118.

BGR (Deutsche Bundesanstalt für Geowissenschaften und Rohstoffe), WAJ (Water Authority of Jordan), 1993. Groundwater resources of Northern Jordan. Structural features of the main hydrogeological units in Northern Jordan, vol 3. BGR-Archive No. 112708, Amman, Jordan.

BGR (Deutsche Bundesanstalt für Geowissenschaften und Rohstoffe), WAJ (Water Authority of Jordan), 2001. Groundwater Resources of Northern Jordan – Contributions to the Hydrology of Northern Jordan, vol. 4. Ministry of Water and Irrigation, Amman, Jordan

Blessent, D., Jørgensen, P.R., Therrien, R., 2014. Comparing Discrete Fracture and Continuum Models to Predict Contaminant Transport in Fractured Porous Media. Groundwater, 52(1), 84-95.

Chen, W., Ghaith, A., Park, A., Ortoleva, P., 1990. Diagenesis through coupled processes: Modeling approach, self-organization, and implications for exploration. In: Meshri, I., Ortoleva, P. (Eds.), AAPG Memoir 49: Prediction of Reservoir Quality through Chemical Modeling, pp. 103-130.

Diersch, H.-J. G., 2002. FEFLOW Finite-Element Subsurface Flow and Transport Simulation System, User's Manual, Release 6.0. WASY GmbH, Berlin, 2002.

732   Diersch, H.J.G., Kolditz, O., 2002. Variable-density flow and transport in porous
733 media: approaches and challenges. Advances in Water Resources, 25(8–12), 899-
734 944.

735   Eckstein, Y., Simmonsi, G., 1977. Measurement and interpretation of terrestrial
736 heat flow in Israel. Geothermics, 6(3–4), 117-142.

737   Evans, D.G., Nunn, J.A., Hanor, J.S., 1991. Mechanisms driving groundwater flow
738 near salt domes. Geophysical Research Letters, 18(5), 927-930.

739   Flexer, A., 1964. The paleogeography of the Senonian and Maestrichtian in
740 northern Israel. PhD Thesis, Hebrew University, Jerusalem, 157 pp.

741   Garven, G., Bull, S.W., Large, R.R., 2001. Hydrothermal fluid flow models of
742 stratiform ore genesis in the McArthur Basin, Northern Territory, Australia.
743 Geofluids, 1(4), 289-311.

744   Gat, J.R., Mazor, E., Tzur, Y., 1969. The stable isotope composition of mineral
745 waters in the Jordan Rift Valley, Israel. Journal of Hydrology, 7(3), 334-352.

746   Goldshmidt, M.J., Arad, A., Neev, D., 1967. The mechanism of the saline springs
747 in the Lake Tiberias depression. Geological Survey of Israel Bulletin, 45, 1-19.

748   Greitzer, Y., 1980. Hydrodynamic Investigation of Geological Formations in
749 Israel for the Purpose of Oil Exploration: Stage 1. Geological and Hydrological
750 Projects.

751   Gvirtzman, H., Garven, G., Gvirtzman, G., 1997a. Hydrogeological modeling of
752 the saline hot springs at the Sea of Galilee, Israel. Water Resources Research, 33(5),
753 913-926.

754   Gvirtzman, H., Garven, G., Gvirtzman, G., 1997.b Thermal anomalies associated
755 with forced and free ground-water convection in the Dead Sea rift valley. Geological
756 Society of America Bulletin, 109(9), 1167-1176.

757   Hirsch, F., 2005. The Jurassic of Israel. In: J.K. Hall, V.A. Krasheninnikov, F. Hirsch,
758 C. Banjamini, A. Flexer (Ed.), Geological Framework of the Levant, The Levantine
759 Basin and Israel, vol. II, Historical Productions-Hall, Jerusalem, pp. 361-391.

760   Hurwitz, S., Goldman, M., Ezersky, M., Gvirtzman, H., 1999. Geophysical (Time
761 Domain Electromagnetic Model) delineation of a shallow brine beneath a
762 freshwater lake, the Sea of Galilee, Israel. Water Resources Research, 35(12), 3631-
763 3638.

764   Hurwitz, S., Stanislavsky, E., Lyakhovsky, V., Gvirtzman, H., 2000a. Transient
765 groundwater-lake interactions in a continental rift: Sea of Galilee, Israel. Geological
766 Society of America Bulletin, 112(11), 1694-1702.

767   Hurwitz, S., Lyakhovsky, V., Gvirtzman, H., 2000b. Transient salt transport
768 modeling of shallow brine beneath a freshwater lake, the Sea of Galilee, Israel.
769 Water Resources Research, 36(1), 101-107.

770   Inbar, N., 2012. The evaporitic subsurface body of Kinnarot Basin - Stratigraphy,
771 structure, geohydrology. Ph.D Thesis, Tel Aviv University, 131 pp.

772   Ingebritsen, S.E., Sanford, W.E., 1999. Groundwater in geologic processes.
773   Cambridge University Press.

774   Kaudse, T., 2014. Noble gases in groundwater of the Azraq Oasis, Jordan, and
775   along the central Dead Sea Transform - Two case studies Ruperto-Carola University
776   of Heidelberg, Heidelberg 219 pp.

777   Kesler, A., 2011. Hydrological analysis of salt flow into Lake Kinneret.
778   Environmental & Water Resources Engineering (2002) report, (in Hebrew), 61 pp.

779   Klein-BenDavid, O., Sass, E., Katz, A., 2004. The evolution of marine evaporitic
780   brines in inland basins: The Jordan–Dead Sea Rift valley. Geochimica et
781   Cosmochimica Acta, 68(8), 1763–1775.

782   Kolodny, Y., Katz, A., Starinsky, T., Moise, T., Simon, E., 1999. Chemical tracing
783   of salinity sources in Lake Kinneret (Sea of Galilee), Israel. Limnol. Oceanogr., 44,
784   1035-1044.

785   Lapwood, E.R., 1948. Convection of a fluid in a porous medium. Mathematical
786   Proceedings of the Cambridge Philosophical Society, 44(04), 508-521.

787   Levitte, D., Eckstein, Y., 1978. Correlation between the silica concentration and
788   the orifice temperature in the warm springs along the jordan-dead sea rift valley.
789   Geothermics, 7(1), 1-8.

790   Lopez, D.L., Smith, L., 1996. Fluid flow in fault zones: influence of hydraulic
791   anisotropy and heterogeneity on the fluid flow and heat transfer regime. Water
792   Resour Res 32:3227–3235

793   Magri, F., Bayer, U., Maiwald, U., Otto, R., Thomsen, C., 2009. Impact of
794   transition zones, variable fluid viscosity and anthropogenic activities on coupled
795   fluid-transport processes in a shallow salt-dome environment. Geofluids, 9(3), 182-
796   194.

797   Magri, F., Akar, T., Gemici, U., Pekdeger, A., 2012. Numerical investigations of
798   fault-induced seawater circulation in the Seferihisar-Balçova Geothermal system,
799   western Turkey. Hydrogeology Journal, 20(1), 103-118.

800   Makhlouf, I., Abu-Azzam, H., Al-Hiayri, A., 1996. Surface and subsurface
801   lithosratigraphic relationships of the Cretacceous Ajlun Group in Jordan. Subsurface
802   Geology Bolletin No.8, 95 pp.

803   Marcus, E., Slager , J., 1985. The sedimentary-magmatic sequence of the Zemah-
804   1 well (Jordan-Dead Sea Rift, Israel) and its emplacement in time and space,. Isr. J.
805   Earth Sci., 34, 1-10.

806   Mazor, E., Mero, F., 1969. Geochemical tracing of mineral and fresh water
807   sources in the Lake Tiberias Basin, Israel. Journal of Hydrology, 7(3), 276-317.

808   McCaffrey M.A., Lazar B., Holland HD, 1987. The evaporation path of seawater
809   and the coprecipitation of Br^- and K^+ with halite. Journal of Sedimentary Petrology,
810   57, 928–937.

811   McKibbin, R., 1986. Heat transfer in a vertically-layered porous medium heated
812   from below. Transp Porous Med, 1(4), 361-370.

813   Meiler, M., 2011. The Deep Geological Structure of the Golan Heights and the
814   Evolution of the Adjacent Dead Sea Fault System. Ph.D Thesis, Tel Aviv University,
815   153 pp.

816   Mero, F., S. Mandel, 1963. The hydrological mechanism of the saline springs of
817   the western shore of Lake Kinneret (in Hebrew), Rep. 2399, Tahal, Tel-Aviv, 10 pp.

818   Moise, T., Starinsky, A., Katz, A., Kolodny, Y., 2000. Ra isotopes and Rn in brines
819   and ground waters of the Jordan-Dead Sea Rift Valley: enrichment, retardation, and
820   mixing. Geochimica et Cosmochimica Acta, 64, 2371-2388.

821   Möller, P., Siebert, C., Geyer, S., Inbar, N., Rosenthal, E., Flexer, A., Zilberbrand,
822   M., 2012. Relationship of brines in the Kinnarot Basin, Jordan-Dead Sea Rift Valley.
823   Geofluids, 12(2), 166-181.

824   Möller, P., Rosenthal, E., Flexer, A., 2014. The hydrogeochemistry of subsurface
825   brines in and west of the Jordan–Dead Sea Transform fault. Geofluids, 14(3), 291-
826   309.

827   Nield, D.A., 1968. Onset of Thermohaline Convection in a Porous Medium.
828   Water Resources Research, 4(3), 553-560.

829   O'Brien J. J., Lerche I., 1988. Impact of Heat Flux around Salt Diapirs and Salt
830   Sheets in the Gulf Coast on Hydrocarbon Maturity: Models and Observations, Gulf
831   Coast Association of Geological Societies Transactions, 38, pp 231–243.

832   Reznikov, M., Ben-Avraham, Z., Garfunkel, Z., Gvirtzman, H., Rotsteina, Y., 2004
833   Structural and stratigraphic framework of Lake Kinneret. Israel Journal of Earth
834   Sciences Volume 53(3-4), 131-149.

835   Rimmer, A., Hurwitz, S., Gvirtzman, H., 1999. Spatial and temporal
836   characteristics of saline springs: Sea of Galilee, Israel. Ground water, 37(5), 663-73.

837   Rimmer, A., 2000. The influence of lake level on the discharge of the Kinneret
838   saline springs. Advances in Limnology, 55(55–67).

839   Rimmer, A., 2003. The mechanism of Lake Kinneret salinization as a linear
840   reservoir. Journal of Hydrology, 281(3), 173-186.

841   Roded, R., Shalev, E., Katoshevski, D., 2013. Basal heat-flow and hydrothermal
842   regime at the Golan–Ajloun hydrological basins. Journal of Hydrology, 476(0), 200-
843   211.

844   Rosenfeld, A., Hirsch, F., 2005. The Cretaceous of Israel. In: Hall J. K., K.V.A.,
845   Hirsch F., Benjamini Ch, Flexer A. (Ed.), Geological Framework of the Levant (II): The
846   Levantine Basin and Israel. Historical Productions, Hall Publications, Jerusalem,
847   Israel, pp. 393-436.

848   Saltzman, U., 1964. The Geology of Tabcha-Hukok-Migdal region. P.N. 374,
849   Tahal, Tel Aviv.

850   Sarkar, A., Nunn, J.A., Hanor, J.S., 1995. Free thermohaline convection beneath
851   allochthonous salt sheets: An agent for salt dissolution and fluid flow in Gulf Coast
852   sediments. Journal of Geophysical Research: Solid Earth 100(B9), 18085-18092.

853   Severini, A.P., Huntley, D., 1983. Heat Convection in Warm Springs Valley,
854   Virginia. Ground Water, 21(6), 726-732.

855   Shalev, E., Lyakhovsky, V., Yechieli, Y., 2007. Is advective heat transport
856   significant at the Dead Sea basin? Geofluids, 7(3), 292-300.

857   Shalev, E., Levitte, D., Gabay, R., Zemach, E., 2008. Assessment of Geothermal
858   Resources in Israel, the Ministry of National Infrastructures Geological Survey of
859   Israel Jerusalem.

860   Shalev, E., Lyakhovsky, V., Weinstein, Y., Ben-Avraham, Z., 2013. The thermal
861   structure of Israel and the Dead Sea Fault. Tectonophysics, 602(0), 69-77.

862   Shewchuk, J.R., 1996. Triangle: Engineering a 2D Quality Mesh Generator and
863   Delaunay Triangulator. In: Lin, M.C., Manocha, D. (Eds.), Applied Computational
864   Geometry: Towards Geometric Engineering. Springer-Verlag, Berlin, pp. 203-222.

865   Shulman, H., Reshef, M., Ben-Avraham, Z., 2004. The structure of the Golan
866   Heights and its tectonic linkage to the Dead Sea Transform and the Palmyrides
867   folding Isr. J. Earth Sci., 53, 225-237.

868   Siebert, C., Möller, P., Geyer, S., Kraushaar, S., Dulski, P., Guttman, J., Subah, A.,
869   Rödiger, T., 2014. Thermal waters in the Lower Yarmouk Gorge and their relation to
870   surrounding aquifers. Chemie der Erde - Geochemistry, 74, 425-441.

871   Simmons, C.T., Sharp, J.M., Jr, Nield D.A., 2008. Modes of free convection in
872   fractured low-permeability media. Water ResourRes, 44, W03431.

873   Simon, E., Mero, F., 1992. The salinization mechanism of Lake Kinneret. Journal
874   of Hydrology, 138(3–4), 327-343.

875   Stiller, M., Carmi, I., Münnich, K.O., 1975. Water transport through Lake
876   Kinneret sediments traced by tritium. Earth and Planetary Science Letters, 25(3),
877   297-304.

878   Stiller, M., Rosenbaum, J.M., Nishri, A., 2009. The origin of brines underlying
879   Lake Kinneret. Chemical Geology, 262(3–4), 293-309.

880   Tsur, N., 2013. Noble gas isotopic signatures in thermal waters of the Dead Sea
881   Transform, Israel, Ruprecht-Karls-University Heidelberg, Heidelberg, 108 pp.

882   Vengosh, A., Rosenthal, E., 1994. Saline groundwater in Israel: its bearing on the
883   water crisis in the country. Journal of Hydrology, 156(1–4), 389-430.

884   Vujević, K., Graf, T., Simmons, C.T., Werner, A.D., 2014. Impact of fracture
885   network geometry on free convective flow patterns. Advances in Water Resources,
886   71(0), 65-80.

887   Water Authority of Israel, Hydrological Service, 2012. Development of water
888   exploitation and the state of water resources in Israel, Autumn 2011 (in Hebrew),
889   473 pp.

890   Yang, J., 2006. Finite element modeling of transient saline hydrothermal fluids
891   in multifaulted sedimentary basins: implications for ore-forming processes.
892   Canadian Journal of Earth Sciences, 43(9), 1331-1340.

893   Yechieli Y., Shaliv G., Wallman S., Kessler A., Rozenzpet M., Berger D., Bein A.
894   2011. Three dimensional model for the Kalanit Basin (Fuliya and Tabgha basin). GSI
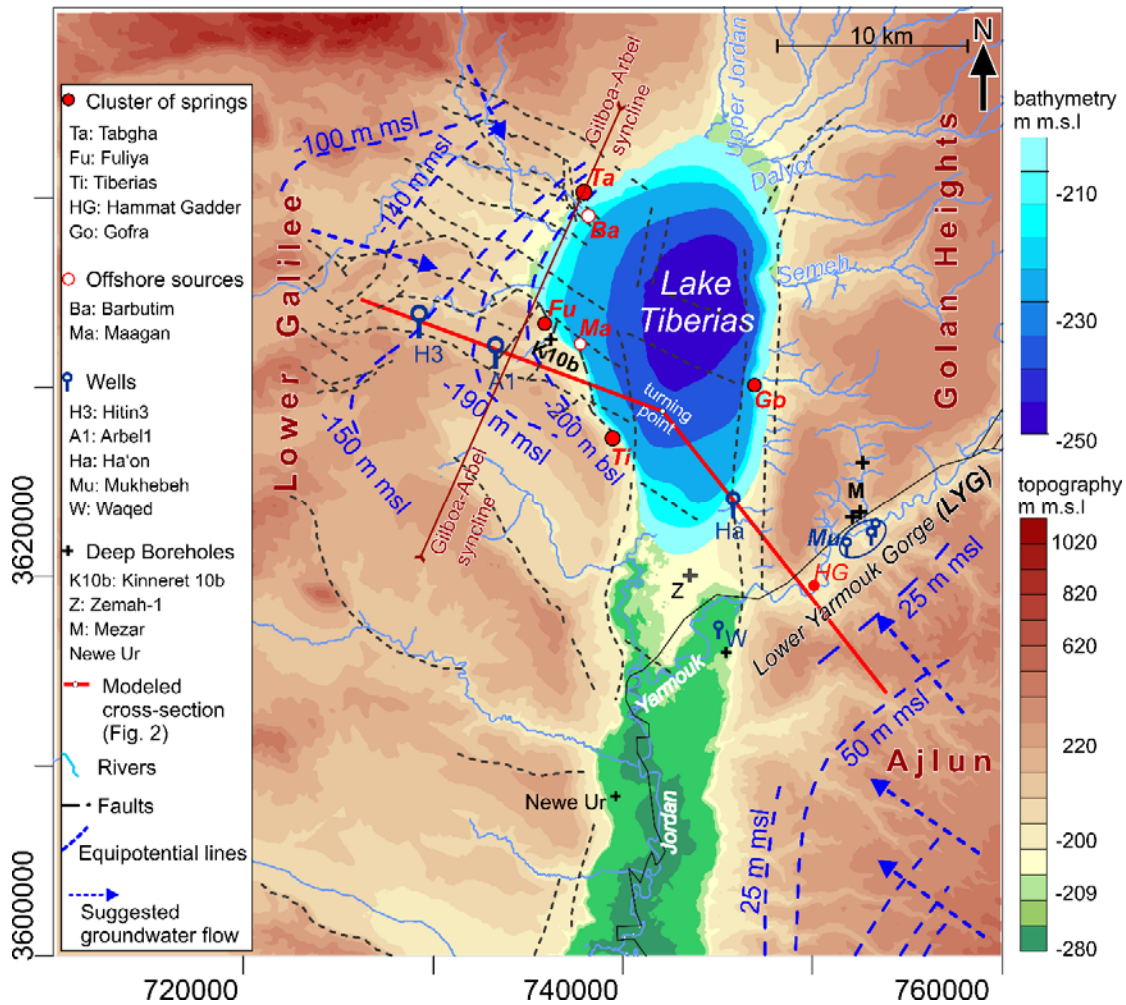895   Project report GSI/38/2011, (in Hebrew), 101 pp.

Fig. 1.The Tiberias Basin (TB). Study area including: location of the modeled cross section (Fig. 2), topography and lake bathymetry (SRTM data, Reuters et al. 2007), major faults (Ben-Avraham et al., 1996; Hurwitz et al.l, 2002c; Reznikov et al., 2004), clusters of springs, wells, deep boreholes, equipotential lines mean sea level (Water Authority of Israel, 2012; BGR 2001) and suggested groundwater flow directions (Bergerlson et al. 1998). **LYG**: Lower Yamourk Gorge.

Location "Cs": cluster of springs, "w" : well, "b": borehole	Abbreviation	TDS (g L^{-1}) range	Temperature (°C) range
Tabgha (Cs)	Ta	2.25 – 5.23 [1]	19 – 29 [1]
Fuliya (Cs)	Fu	2.06 – 2.72 [1,7]	27 – 30 [4,7]
Tiberias Hot Spring	Ti	28.94 [1]	64 [4]
Mukhebeh (Cs)	Mu	0.5 [9]	33 – 43 [9]
Hammat Gader (Cs)	HG	0.64 – 1.22 [1,9]	28 - 50 [1,7]
Gofra (Cs)	Go	5.07 [7]	32 [7]
Hitin 3 (w)	H3	0.48 – 0.517 [6,7]	25.8 [7]
Kinneret 10 (b)	K10b	24.7 – 31.7 [,7]	46 – 52 [7]
Ha'on (w)	Ha	14 – 22.5 [1,7]	24 – 35 [1,7]
Zemah-1 (b)	Z	220	-

Table 1 Range of temperatures, Total Dissolved Solids (TDS) and flow rates for the major cluster of springs (Cs), wells (w) and boreholes (b) as located in figure 1. The values are adapted from selected publications (superscript number) and do not provide a strict minimum-maximum interval.
1 - Möller et al. (2012), 2 - Abbo et al. (2003), 3 - Water Authority of Israel (2012), 4 - Gvirtzman et al. (1997a, 1997b), 5 - Rimmer (2003), 6 - Bergelson et al. (1998), 7 - Bergelson et al. (1999), 8 - Levitte and Eckstein (1978), 9 – Baijjali et al. (1997)
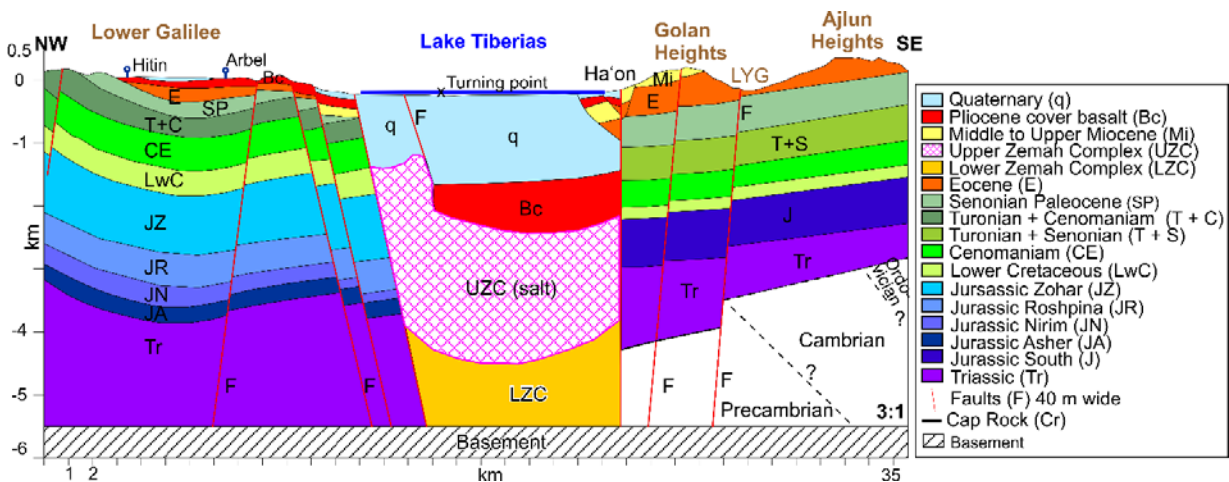

Fig. 2. Representative NW-SE cross section from Upper Galilee (Israel) to the Ajlun (Jordan) including wells and Lower Yarmouk Gorge (LYG) locations. Vertical exaggeration 3:1. Based on Saltzman et al. (1964), BGR (1993), Inbar (2012), Meiler (2011). In the southern ending of the profile, question mark symbols (?) refer to geological features that remain poorly constrained and are not implemented in the numerical model. The presence of a fault in the LYG is still debated. The physical properties of the different units and their values are listed in Table 2.

Epoch		Unit abbreviation	Segment of the profile (NW - SE)	Formation	Lithology	kx,y (m/yr)	storage 10⁻⁶ (1/m)	Poro (I)	Heat cond (W/m/K)
Quaternary	Holocene Pleistocene	Q		Dead Sea Gr.	Dead sea silt, marl, mudstone, sandstone	0.5	2.0	0.2	1.3
Tertiary	Pliocene	Bc		Cover basalt	mostly basalt, sediments	2 - 10	1.0	0.05	1.7
	Miocene	UZC		Upper Zemah Complex	mostly salt	imp.	0.2	0.01	3.6
		LZC		Lower Zemah Complex	mostly gabro & carbonate	0.010	0.2	0.01	2.1
		M		Hordos Fm.	conglomerates	5.0	1.6	0.08	2.1
	Eocene	E		Avedat Gr.	limstones	10.0	1.0	0.05	2.1
	Senonian	SP	NW	Mt. Scopus Gr.	chalk & marl - aquitard	0.5	2.0	0.1	1.5
		SP	SE	Muwaqqar Fm.	chalk & marl - aquitard	1.0	1.6		1.5
Upper Cretaceous	Upper Cenomanian - Turonian	T+C	NW	Bina & Sakhnin Fm.	limestone	200.0	3.0	0.15	2.1
	Turonian - Senonian	T+S	SE	B2-A7 (Wadi es Sir, Wadi um Ghudran, Amman silicified limestone, Al Hasa Fms.)	mainly limestone - Aquifer	73.0	2	0.1	2.1
	Cenomanian	CE	NW	Dier Hanna	limestone, dolomite interbedded with marls - aquitard	50	2.0	0.1	2.3
				Kamon	dolomite (some marls) - aquifer				
				Shueib	marly limestone - Aquitard				
		CE	SE	Hummar	dolomitic limestone- Aquifer	36.5	3.0	0.15	2.5
				Fuheis	marl - Aquitard				
				Na'ur	marly limestone - Aquifer				
Lower Creataceous		LwC	NW	Kurnub Gr., Hatira, Taysar basalt	Basalt and sandstone	6	1.6	0.08	2.2
		LwC	SE	Nebi Said	mostly permeable sandstone	110	3.0	0.15	
Jurassic		JZ		Zohar, Haluza, Sderot	limestone and dolomite	10	1.0	0.05	2.8
		JR	NW	Rosh Pina	marl	0.1	0.6	0.03	2
		JN		Nirim	limestone and dolomite	10	1.0	0.05	2.8
		JA		Asher	basalt and pyroclastics	5	1.6	0.08	2.2

J	SE	Azab	primarily composed of limstones, interbedded with marls	22	0.8	0.04	2.5
Triassic	Tr			0.01	0.2	0.01	2.7
Permian	Basement	Zenifim	Arkose	imp.	0.2	0.01	2.5
	F	Faults	equivalent porous media	29 - 140	4.0	0.2	1.1

Table 2 Units, stratigraphy and values of the physical parameters of the modeled units. The stratigraphy is based on Inbar (2012) and BGR –WAJ reports (1993). The assigned values are adapted from Gvirtzman et al. (1997a, 1997b), Bergelson et al. (1998), Shalev et al. (2007, 2013), Roded et al. (2013).
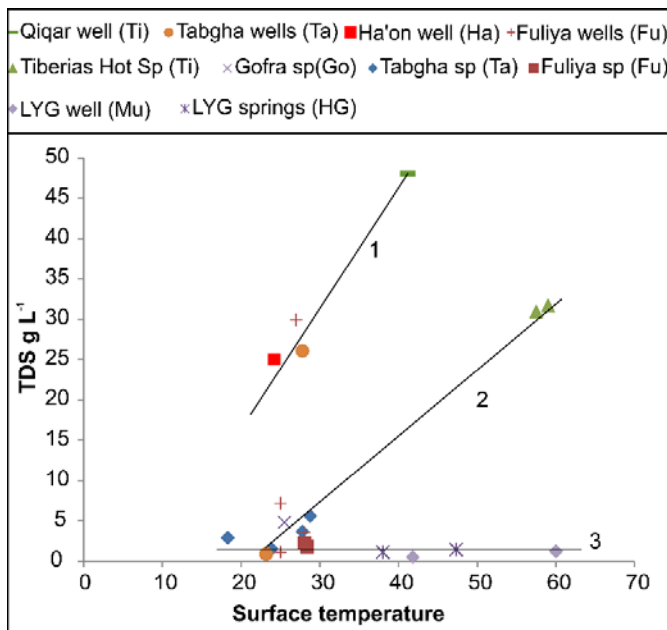
Fig. 3 TDS vs surface temperature correlations for deep wells (1), springs along the lakeshore (2), LYG springs and wells (data after Möller at al., 2014). For locations, refer to figure 1. Qiqar well belongs to the Tiberias cluster of springs.
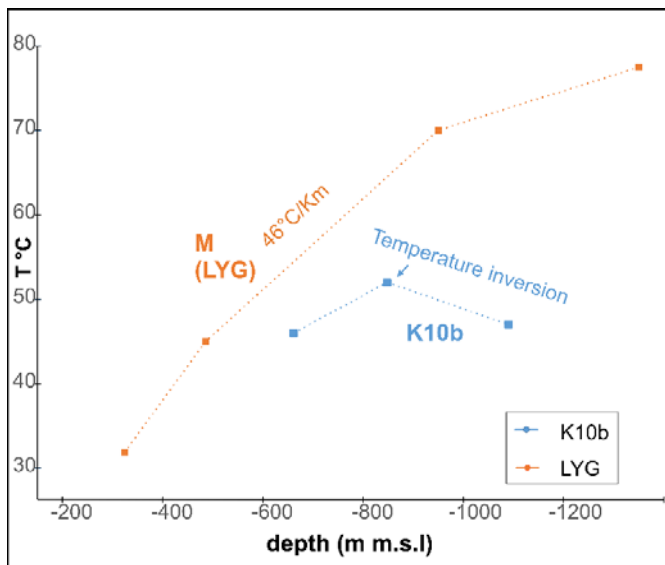
Fig. 4. Temperature profile in the Mezar (M) in the LYG (Roded et al. 2013) and in the Kinnereth 10b (K10b) boreholes (Michelson et al., 1995). The studied profile crosses the LYG at approximately -150 m msl, K10b wellhead is at -208 m m.s.l. Linear interpolations (dashed lines) do not represent the actual temperature trends. The geothermal gradient for the Kinnereth borehole is estimated by Gvirtzman et al. (1997b).
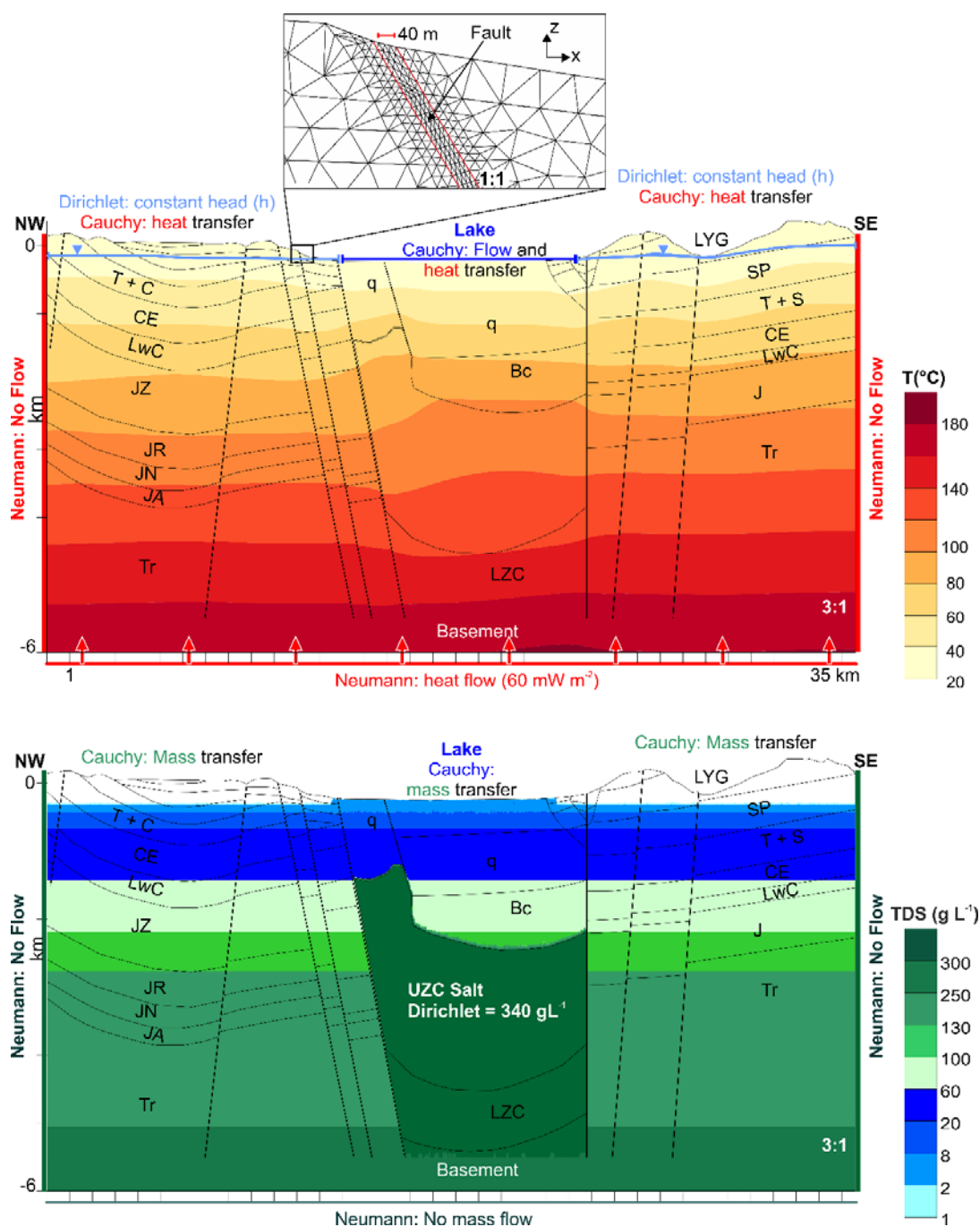
Fig. 5: Boundary and initial conditions. **Top:** Initial temperature (T) distribution (filled contours, in °C) with applied flow and temperature boundary conditions (blue and red lines). Vertical exaggeration 3:1. The local zoom (no vertical exaggeration) shows the triangular finite-element mesh in the fault (40 m wide) and surrounding units. Local refinements ensure that at least four elements discretize the whole fault in the X direction. **Bottom**: Initial TDS (C) distribution (filled contours, in gL^{-1}) with applied mass boundary conditions (green lines). This salinity profile initiates the transient thermohaline simulations described in paragraph 4.2. It represents an imaginary source brine (SB) resulting from relic evaporated seawater that saturates the units. Salinity constraints are based on the geochemical data given in paragraph 2.2. Vertical exaggeration 3:1. For units abbreviations, refer to figure 2 and Table 2
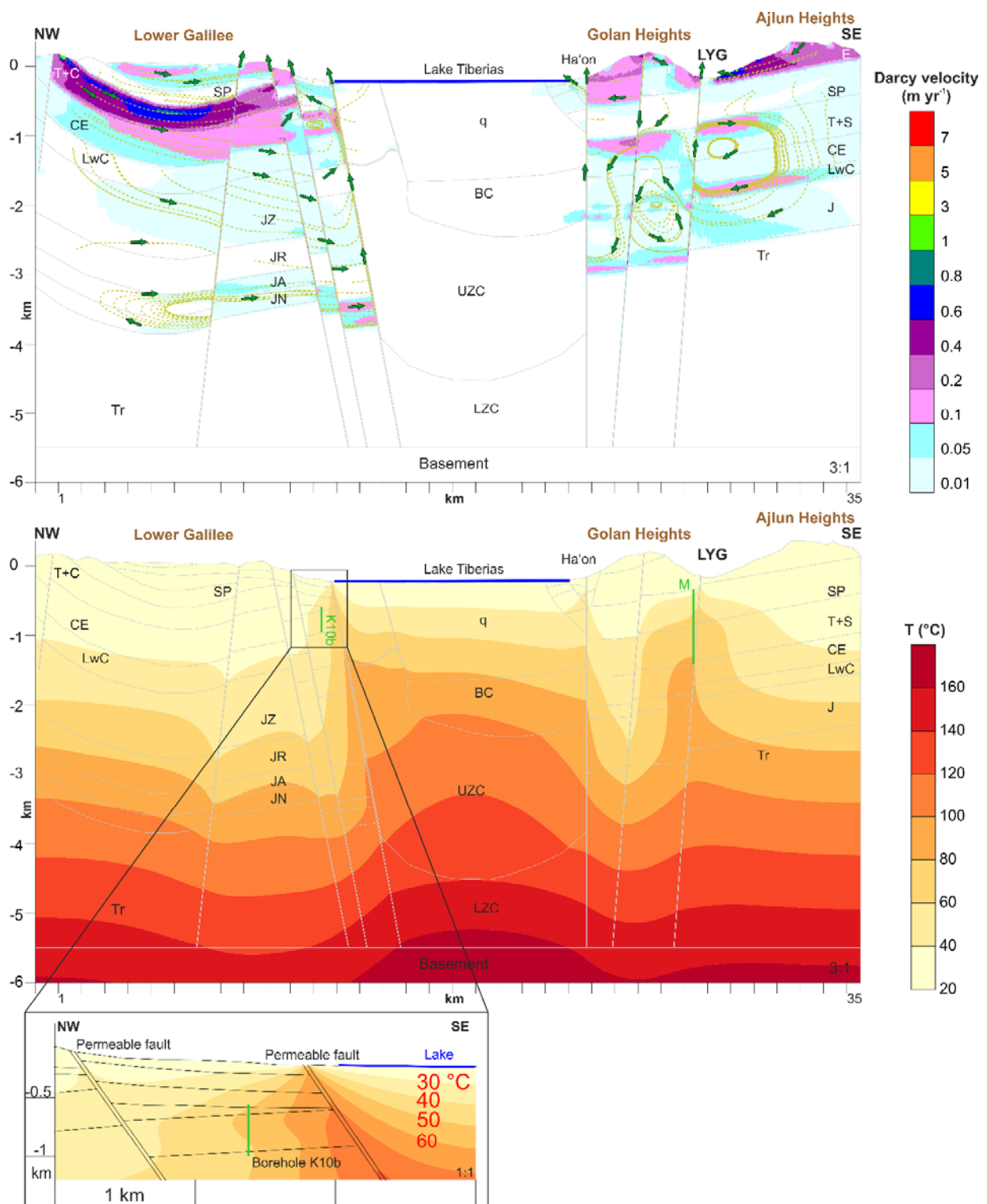
Fig. 6: Scenario 4.1 without salinity effects. **Top** – Colored patterns represent the velocity field (Darcy flow in meter per year) and green dashed lines indicate flow paths (no streamline). Arrows show flow direction. No flow lines are plotted in low velocity field (i.e. lower than 1 cm yr^{-1}). **Bottom** – Calculated temperature profile (°C). Green vertical lines locate two boreholes based on the depths of the Kinnereth 10b (K10b) and Mezar (M, in the LYG) deep wells. The temperature-depth profiles of these two boreholes are illustrated in Fig. 7. The zoom shows the lateral spread of the heat plume due to the presence of a parallel permeable fault.
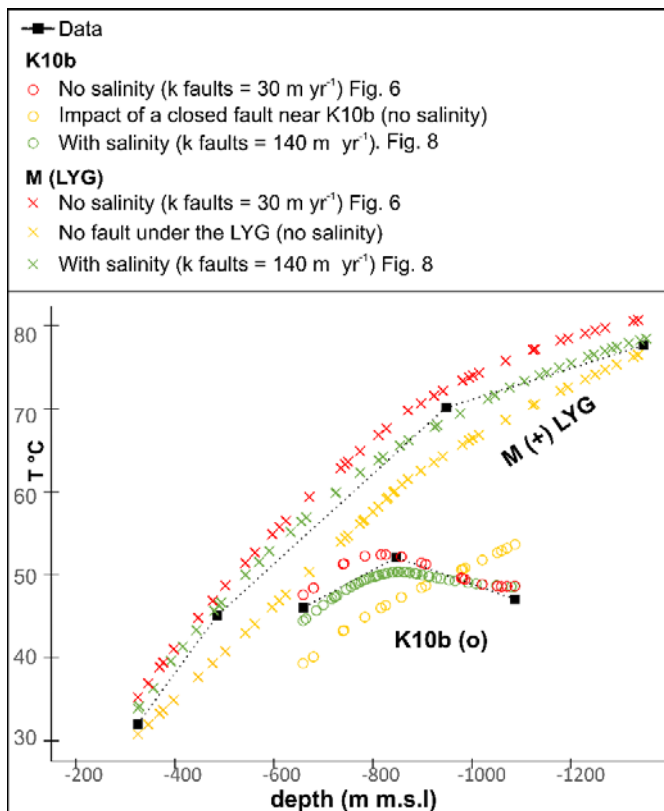
Fig. 7. Calculated temperature-depths at northern (K10b, circles) and southern (M, crosses) sides of the profile compared to field data (squares, Fig. 4). The boreholes are located in Fig.6, bottom and Fig. 8. These putative boreholes are just an illustrative example based on real depths, to show the different temperature trends. Red: scenario in which mass transport is not computed (i.e. no salinity effects, section 4.1). The hydraulic conductivity of the faults is 30 m yr^{-1}. Green: scenario with brine transport (section 4.2) is 140 m yr^{-1}. Yellow: impact of a closed fault near K10b and absence of the fault in the LYG, no buoyancy from salinity effects.
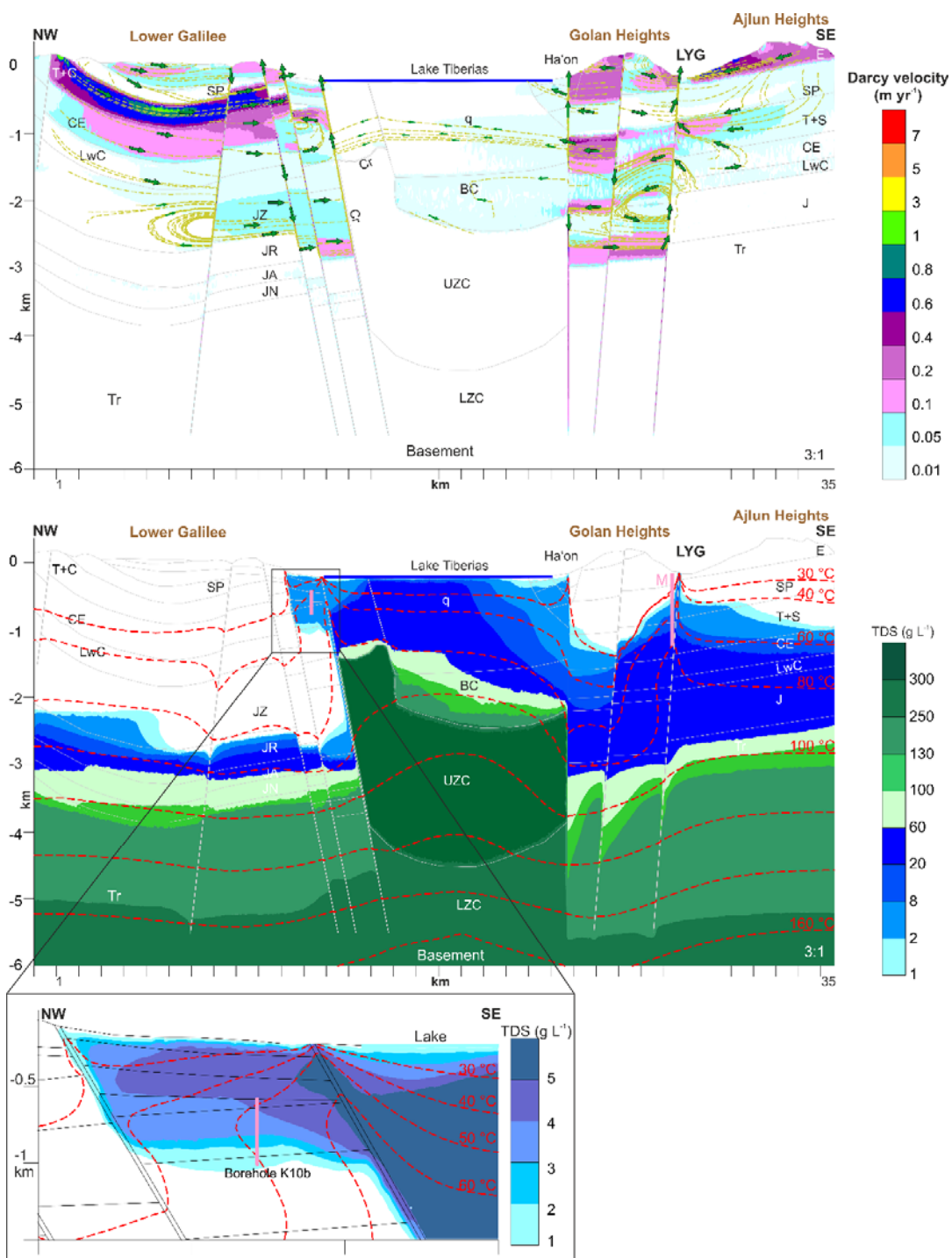
Fig. 8: Scenario 4.2 showing the effects of salinity. **Top** – Colored patterns represent the velocity field (Darcy flow in meter per year) and green dashed lines indicate flow paths (no streamline). Arrows show the flow direction. No flow lines are plotted in low velocity field (i.e. lower than 1 cm yr^{-1}). Small arrows in the sedimentary fill below the lake further highlight the very low velocity field. **Bottom** – Calculated TDS (gL^{-1}) of the source brine distribution and temperature profile (°C, red dashed lines). Heavy brine from the salt diapir (UZC) remains deep-seated, as explained in the section "Impact of salt diapir and faulted lakebed". Pink vertical lines locate two boreholes based on the depths of the Kinnereth 10b (K10b) and Mezar (M, in the LYG) deep wells. The temperature-depth profiles of the two boreholes are illustrated in Fig. 7. The zoom shows the lateral spread of the heat and brine plume due to the presence of a parallel permeable fault.